Supershear rupture in a M_W 6.7 aftershock of the 2013 Sea of Okhotsk earthquake

Zhongwen Zhan *et al.*

Science **345**, 204 (2014);
DOI: 10.1126/science.1252717

Science (print ISSN 0036-8075; online ISSN 1095-9203) is published weekly, except the last week in December, by the American Association for the Advancement of Science, 1200 New York Avenue NW, Washington, DC 20005.

REFERENCES AND NOTES

1. S. L. Johnson, E. Vorobeva, P. Beaud, C. J. Milne, G. Ingold, *Phys. Rev. Lett.* **103**, 205501 (2009).
2. V. Juvé *et al.*, *Phys. Rev. Lett.* **111**, 217401 (2013).
3. D. M. Fritz *et al.*, *Science* **315**, 633–636 (2007).
4. B. J. Siwick, J. R. Dwyer, R. E. Jordan, R. J. D. Miller, *Science* **302**, 1382–1385 (2003).
5. P. Baum, D.-S. Yang, A. H. Zewail, *Science* **318**, 788–792 (2007).
6. M. Eichberger *et al.*, *Nature* **468**, 799–802 (2010).
7. A. H. Zewail, *Science* **328**, 187–193 (2010).
8. T. LaGrange *et al.*, *Ultramicroscopy* **108**, 1441–1449 (2008).
9. O. F. Mohammed, D.-S. Yang, S. K. Pal, A. H. Zewail, *J. Am. Chem. Soc.* **133**, 7708–7711 (2011).
10. M. Chergui, *Acta Crystallogr. A* **66**, 229–239 (2010).
11. F. Carbone, O.-H. Kwon, A. H. Zewail, *Science* **325**, 181–184 (2009).
12. J. M. Kosterlitz, D. J. Thouless, *J. Phys. Chem.* **6**, 1181–1203 (1973).
13. P. M. Chaikin, T. C. Lubensky, *Principles of Condensed Matter Physics* (Cambridge University Press, Cambridge, 2000).
14. A. Hanisch-Blicharski *et al.*, *Ultramicroscopy* **127**, 2–8 (2013).
15. M. A. Van Hove, W. H. Weinberg, C.-M. Chan, *Low-Energy Electron Diffraction* (Springer, Berlin Heidelberg, 1986).
16. S. Schäfer, W. Liang, A. H. Zewail, *J. Chem. Phys.* **135**, 214201 (2011).
17. R. S. Becker, G. S. Higashi, J. A. Golovchenko, *Phys. Rev. Lett.* **52**, 307–310 (1984).
18. C. Cirelli *et al.*, *Europhys. Lett.* **85**, 17010 (2009).
19. R. Karrer, H. J. Neff, M. Hengsberger, T. Greber, J. Osterwalder, *Rev. Sci. Instrum.* **72**, 4404 (2001).
20. M. Krüger, M. Schenk, P. Hommelhoff, *Nature* **475**, 78–81 (2011).
21. G. Herink, D. R. Solli, M. Gulde, C. Ropers, *Nature* **483**, 190–193 (2012).
22. A. Paarmann *et al.*, *J. Appl. Phys.* **112**, 113109 (2012).
23. E. Quinonez, J. Handali, B. Barwick, *Rev. Sci. Instrum.* **84**, 103710 (2013).
24. J. C. H. Spence, T. Vecchione, U. Weierstall, *Philos. Mag.* **90**, 4691–4702 (2010).
25. H. Park, J. M. Zuo, *Appl. Phys. Lett.* **94**, 251103 (2009).
26. Materials and methods are available as supplementary materials on *Science* Online.
27. R. K. Raman, Z. Tao, T.-R. Han, C.-Y. Ruan, *Appl. Phys. Lett.* **95**, 181108 (2009).
28. M. Tress *et al.*, *Science* **341**, 1371–1374 (2013).
29. J. A. Forrest, K. Dalnoki-Veress, *Adv. Colloid Interfac.* **94**, 167–195 (2001).
30. O. M. Braun, Y. S. Kivshar, *The Frenkel-Kontorova Model: Concepts, Methods, and Applications* (Springer, Berlin, Heidelberg, 2004).
31. A. N. Rissanou, V. Harmandaris, *J. Nanopart. Res.* **15**, 1589 (2013).
32. Y.-C. Lin *et al.*, *Nano Lett.* **12**, 414–419 (2012).
33. A. K. Geim, I. V. Grigorieva, *Nature* **499**, 419–425 (2013).
34. J. Kumaki, T. Kawauchi, E. Yashima, *J. Am. Chem. Soc.* **127**, 5788–5789 (2005).
35. J. S. Ha *et al.*, *J. Vac. Sci. Technol. B* **12**, 1977–1980 (1994).
36. Whereas the (10) diffraction spot of PMMA overlaps with that of graphene, the (3/2 0) PMMA spot is not observed, which is most likely a result of the chain form factor or disorder.

ACKNOWLEDGMENTS

We thank M. Müller for helpful discussions on polymer dynamics. Supporting sample characterizations by H. Schuhmann, M. Seibt, S. Strauch, H. Stark (TEM imaging), S. Dechert, and M. Sivis (Raman spectroscopy), as well as James E. Evans and Nigel D. Browning (high-resolution TEM, Pacific Northwest National Laboratory), are gratefully acknowledged. This work was partially funded by the Deutsche Forschungsgemeinschaft (DFG-ZuK 45/1 and DFG-SFB 1073). M.G. was financially supported by the German National Academic Foundation. A.M.W. and H.K.Y. gratefully acknowledge support from the Alexander von Humboldt Foundation.

SUPPLEMENTARY MATERIALS

www.sciencemag.org/content/345/6193/200/suppl/DC1
Materials and Methods
Figs. S1 to S8
References (*37*–*48*)

9 January 2014; accepted 22 May 2014
10.1126/science.1250658

EARTHQUAKE DYNAMICS

Supershear rupture in a M_w 6.7 aftershock of the 2013 Sea of Okhotsk earthquake

Zhongwen Zhan,[1,2]* Donald V. Helmberger,[2] Hiroo Kanamori,[2] Peter M. Shearer[1]

Earthquake rupture speeds exceeding the shear-wave velocity have been reported for several shallow strike-slip events. Whether supershear rupture also can occur in deep earthquakes is unclear, because of their enigmatic faulting mechanism. Using empirical Green's functions in both regional and teleseismic waveforms, we observed supershear rupture during the 2013 moment magnitude (M_w) 6.7 deep earthquake beneath the Sea of Okhotsk, an aftershock of the large deep earthquake (M_w 8.3). The M_w 6.7 event ruptured downward along a steeply dipping fault plane at an average speed of 8 kilometers per second, suggesting efficient seismic energy generation. Comparing it to the highly dissipative 1994 M_w 8.3 Bolivia earthquake, the two events represent end members of deep earthquakes in terms of energy partitioning and imply that there is more than one rupture mechanism for deep earthquakes.

Most earthquakes rupture at speeds less than the shear-wave speed (V_S). Theory and laboratory experiments indicate that rupture speeds in excess of V_S are possible (*1*–*3*), and supershear ruptures have now occasionally been reported for large strike-slip events (mode II), including the 1979 Imperial Valley (*4*), 1999 Izmit (*5*), 2001 Kunlun (*6*–*8*), 2002 Denali (*7*, *9*), 2010 Yushu (*10*), and 2013 Craig (*11*) earthquakes. All of these documented occurrences were shallow earthquakes with a simple fault geometry (*12*), and mostly with surface breaks, which is consistent with theoretical studies that the free surface helps promote supershear rupture (*13*, *14*).

No definitive evidence has yet been obtained for supershear rupture in deep earthquakes (depth > 300 km) (*15*). However, the rupture speeds of these events are difficult to estimate because of a general absence of near-field observations, and they appear highly variable. For example, the rupture speeds of the two largest deep earthquakes observed to date, the 1994 moment magnitude (M_w) 8.3 Bolivia earthquake and the 2013 M_w 8.3 Sea of Okhotsk earthquake (*16*–*18*), were about 0.2 to 0.4 and 0.7 V_S, respectively. About 80% of the rupture velocities for deep earthquakes fall between 0.3 and 0.9 V_S (*19*), a greater range than is seen for shallow earthquakes (*15*). The rupture speed may depend on the slab thermal state (*20*, *21*), with ruptures propagating more slowly in warm slabs than in cold slabs, but seismic observations have been inconclusive (*22*, *23*). The one previous example of observed supershear rupture during the 1990 M_w 7.1 Sakhalin deep earthquake neglected to take into account waveform changes from attenuation and the high-velocity subducted slab (*24*, *25*).

The 24 May 2013 M_w 8.3 Sea of Okhotsk event (depth, 607 km) was the largest deep earthquake ever recorded (Fig. 1), slightly larger than the 1994 Bolivia earthquake. On the same day, an M_w 6.7 earthquake at a depth of 642 km occurred about 300 km southwest of the mainshock and was recorded by many teleseismic stations and one regional station (Fig. 1). An extraordinary feature of the M_w 6.7 event was its sharp teleseismic *P* waves, which had displacement pulse widths at most azimuths of 1 to 2 s (Fig. 1). These are much less than the expected source duration of 8 s, based on its magnitude and previous studies of scaled durations of deep earthquakes (*26*, *27*). If taken as a rough estimate of the M_w 6.7 earthquake's source duration, these very short teleseismic *P*-wave durations imply extremely high stress drops in a range from 157 MPa to 5.856 GPa (*17*). On the other hand, the regional station PET (distance ≈ 495 km) on the Kamchatka Peninsula to the east displayed a much longer direct *P* wavetrain of about 5 s (Fig. 1). Because the *P* wave to the PET station left the source along an upgoing ray path, instead of the downgoing rays for the teleseismic stations, this longer *P*-wave duration at PET suggests possible downward rupture directivity during the M_w 6.7 earthquake. However, to test this possibility we first need to account for possible path effects such as wave diffractions along the high-velocity slab in which the earthquake occurred and site effects at the stations.

We used waveforms from two nearby smaller earthquakes (Fig. 1; the 24 June 2013 M_w 4.3

[1]Institute of Geophysics and Planetary Physics, Scripps Institution of Oceanography, University of California, San Diego, La Jolla, CA 92093–0225, USA. [2]Seismological Laboratory, California Institute of Technology, 1200 East California Boulevard, Pasadena, CA 91125, USA.
*Corresponding author. E-mail: zwzhan@ucsd.edu, zwzhan@gmail.com

event and the 30 August 1996 M_w 5.5 event) as empirical Green's functions (EGFs) to calibrate the paths. The M_w 4.3 earthquake's small moment, similar depth, and probably similar focal mechanism as the M_w 6.7 earthquake (fig. S1) make it an ideal EGF event. Its direct *P* wave recorded at the PET station displays two distinct arrivals separated by about 2 s (Fig. 2), due to diffraction along the dipping high-velocity slab in the upper mantle (*25*). Therefore, the apparent 5-s *P* duration of the M_w 6.7 earthquake at the PET station was partly caused by the structural path effect. We deconvolved the EGF waveform from the M_w 6.7 earthquake *P* wave to remove the path effect and obtained a more accurate source-time function (STF) (*28*). Most of the energy then concentrated in the first ~2 s, which we measured as the STF duration at the PET station (Fig. 2; red shading in top STF).

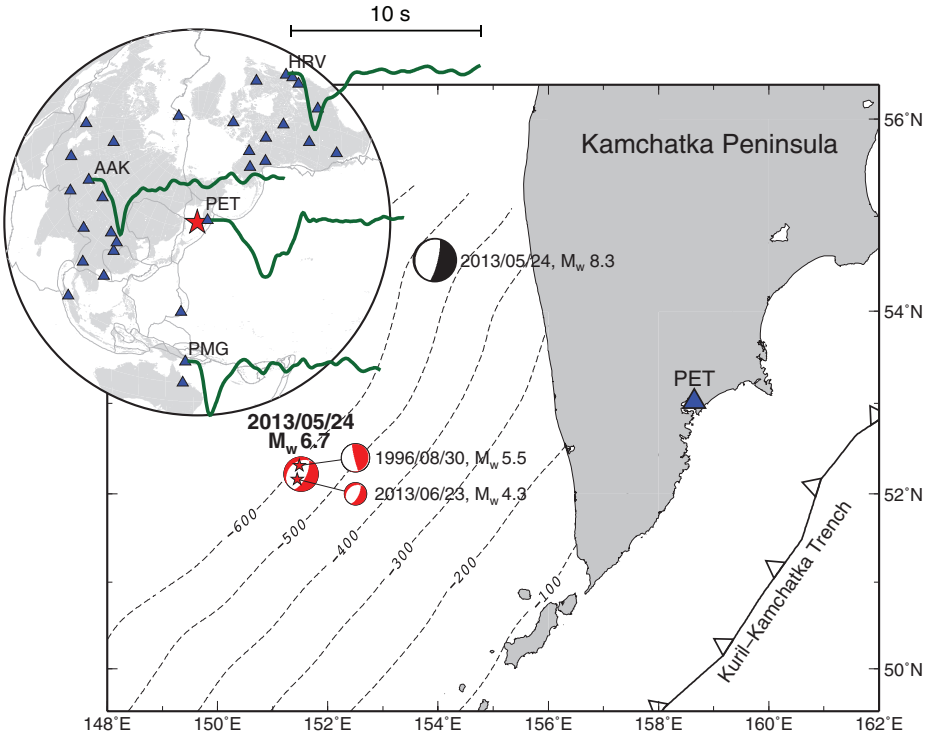

Fig. 1. Earthquake and station locations. The 2013 Okhostk M_w 8.3 mainshock and M_w 6.7 aftershock are displayed as the black and red beachballs, respectively. The two red stars connected with two smaller beachballs represent the EGF events used in this study. Slab contours from the Slab 1.0 model (*31*) are shown as dashed lines. The inset shows teleseismic and regional stations with four representative *P* vertical displacement seismograms (green lines).

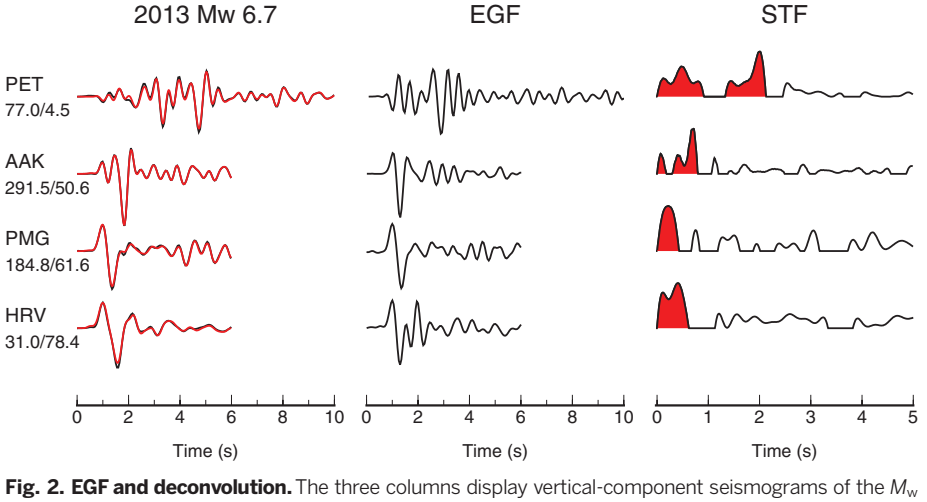

Fig. 2. EGF and deconvolution. The three columns display vertical-component seismograms of the M_w 6.7 earthquake, EGFs, and the deconvolved STFs. To ensure high signal-to-noise ratio and enhance high-frequency energy, we used acceleration seismograms filtered between 0.5 and 1 Hz. Seismograms of the M_w 6.7 event and EGFs are flipped to have the same polarity before deconvolution. The black and red traces in the first column are the data and predictions, respectively. The two numbers beneath station names are distances and azimuths in degrees. In the third column, we show the STF durations defined by the red shading, which includes most of the energy.

Because teleseismic records of the M_w 4.3 event are noisy, we used the 1996 M_w 5.5 event at somewhat shallower depth (~590 km) with a slightly rotated focal mechanism (Fig. 1) as the teleseismic EGF event. Because we only used teleseismic direct *P* waveforms (no absolute amplitude), these small differences in depth and radiation pattern did not significantly affect the accuracy of the EGFs. The M_w 4.3 and 5.5 EGF events had highly similar waveforms at the regional station PET and several quiet teleseismic stations (fig. S2), despite their difference in moment. This suggests that both EGF events can be regarded as delta-function–like point sources and their waveforms are mostly controlled by path effects. We chose teleseismic stations with clean direct *P* waves from both the M_w 6.7 and the M_w 5.5 earthquakes (Fig. 1 inset) and then deconvolved to estimate STFs and their durations (Fig. 2 and fig. S3). The resulting teleseismic STF durations range from ~0.5 to ~1 s. For both regional and teleseismic stations, relatively simple and compact STFs convolved with the EGFs produce good fits to the direct *P* and *P*-coda waveforms of the M_w 6.7 earthquake, which suggests effective correction of the path effects. We also attempted to include two more stations, MA2 and YSS, at distances of about 818 and 858 km, respectively (fig. S4). Direct *P* waves from these stations left the source along approximately horizontal ray paths. However, because of waveform complexities caused by triplications due to the 660-km discontinuity (figs. S4 to S6), we were unable to find an appropriate EGF event to correct for these structural effects.

After removing the path effects with EGFs, we inverted the resulting STF durations for earthquake rupture parameters. The path-corrected STF duration of the PET station (~2.1 s) is still more than two times longer than those of the teleseismic stations (0.5 to ~1 s), suggesting downward rupture directivity. For three-dimensional unilateral rupture (fig. S7), the STF duration of the *i*-th station T_i can be written as a function of rupture duration τ, horizontal rupture azimuth θ_r, and horizontal and vertical dimensions L and H, as $T_i = \tau + x_i(\theta_r)L + \eta_i H$, where $x_i(\theta_r)L$ and $\eta_i H$ are the corrections for azimuthal and vertical directivity, respectively. Note that $x_i(\theta_r) = -\frac{\cos(\theta_i - \theta_r)}{c_p^i}$ is the horizontal directivity parameter for the *i*-th station with azimuth θ_i and *P*-wave phase velocity $c_p^i = \frac{\alpha}{\sin\varphi_i}$ (*18, 29*). Here φ_i is the takeoff angle for the *i*-th station, and α is the *P*-wave speed. Therefore, the azimuthal variations in STF durations resolve the rupture direction θ_r and horizontal extent L. In the final term, $\eta_i = -\frac{\alpha}{\cos\varphi_i}$ is the vertical slowness, negative for teleseismic stations (with down-going rays) and positive for regional stations (with up-going rays). This sign

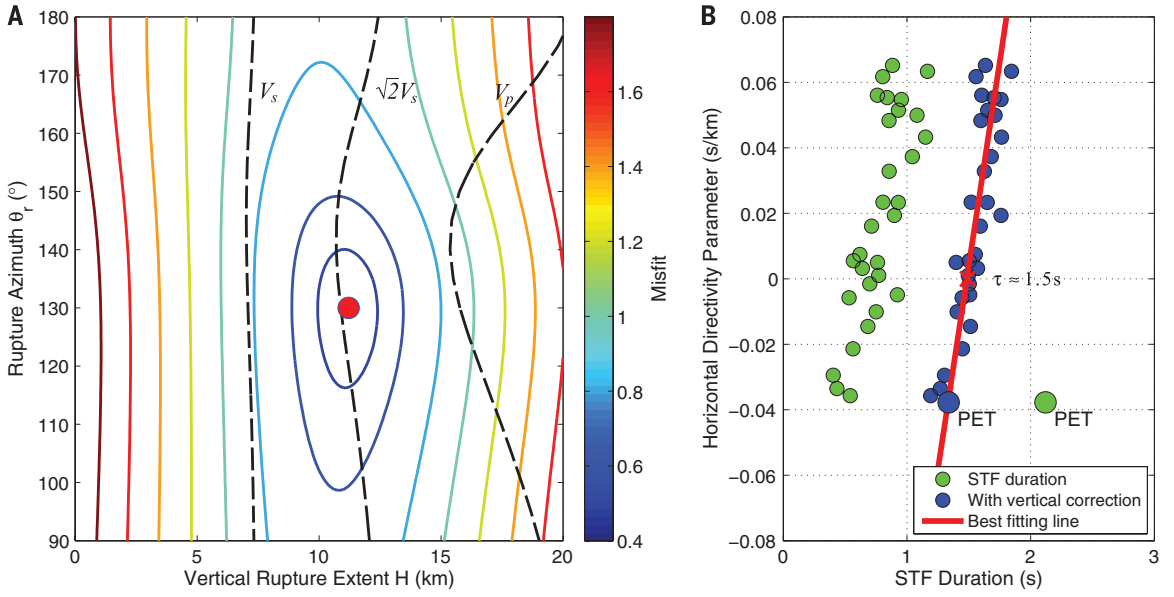

Fig. 3. Inversion for earthquake rupture parameters. (**A**) Misfit as a function of the grid-searched vertical rupture extent H and rupture azimuth θ_r. The red dot at (11 km, 130°) marks the optimal solution without a substantial tradeoff. The dashed contours show the rupture speeds for all grid-searched solutions at reference speeds of V_S, $\sqrt{2}\,V_S$, and V_P. (**B**) STF durations with and without vertical directivity corrections, assuming the optimal values from (A). The corrected STF durations (blue dots) fall near a straight line with a slope of L = 4 km, and zero-crossing duration of τ = 1.5 s (red cross). The green dots show the STF durations without the vertical directivity corrections, in which the PET station has a longer STF duration than all the teleseismic stations.

difference in η_i accounts for the major observed difference between teleseismic and regional STF durations.

We used a grid-search method to invert for the rupture parameters (τ, θ_r, L, and H). The least-squares misfit of the STF durations, as a function of rupture vertical extent H and rupture azimuth θ_r, has a well-defined global minimum at H = 11 km and θ_r = 130° (Fig. 3A). With these optimal values, the STF durations corrected for the downward vertical directivity (Fig. 3B) fall near a straight line with a slope of L = 4 km and zero-crossing duration of τ = 1.5 s. With L = 4 km and H = 11 km, we estimated the rupture dip to be ~70°, coincident with the steeper fault plane's dip of ~69° (*17*). Because the rupture direction θ_r = 130° is roughly perpendicular to the fault strike (~26°), we conclude that the M_w 6.7 earthquake features a downward mode II rupture on the fault plane dipping steeply to the southeast (Fig. 4A). The rupture propagated $\sqrt{L^2+H^2}$ or ~12 km in τ = 1.5 s, from which we estimate an average rupture speed of about 8 km/s. This speed is about $\sqrt{2}\,V_S$, which is substantially higher than the local shear wave speed (V_S ~5.5 km/s, based on the Preliminary Reference Earth Model). Contouring the average rupture speeds for all grid-searched rupture parameters (Fig. 3A) shows that within the region with reasonable misfit (inside the dark blue contours), the rupture speed is always higher than V_S and lower than V_P. Within 95% confidence limits, the average rupture speed is 8.0 ± 0.7 km/s. Anomalously broad teleseismic depth phases (*pP*) also are roughly consistent with the downward supershear rupture model (figs. S8 and S9). However, *pP* pulse widths exhibit much larger scatter than *P* pulse widths, and their behavior appears to be heavily influenced by complicated path effects, thus we cannot invert the *pP* waveforms for rupture parameters with any confidence.

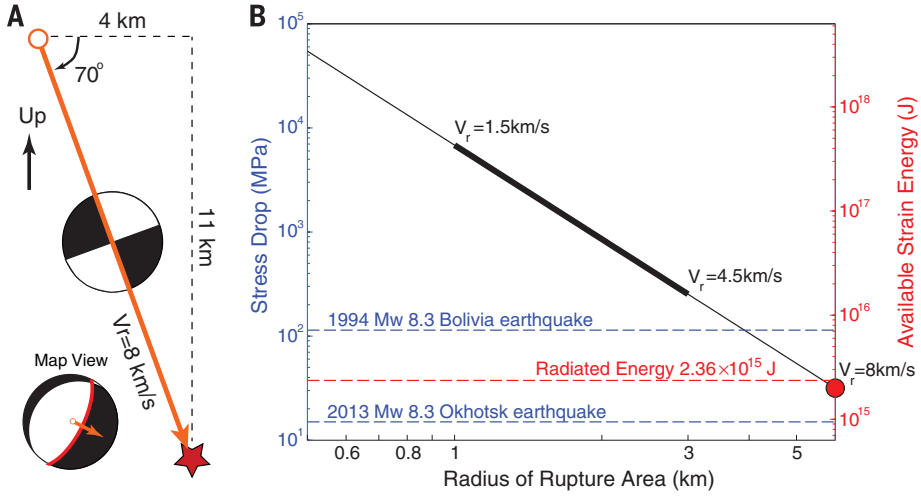

Fig. 4. Earthquake stress drop and energy partitioning. (**A**) Rupture geometry of the M_w 6.7 earthquake. In the focal mechanism in map view, the thick red line marks the steep fault plane on which the rupture is inferred to occur. The orange arrow shows the estimated rupture direction, almost perpendicular to the fault strike. In the side view along the fault strike from the southwest, the earthquake ruptured along the steeper fault plane downward at a speed of 8 km/s. The horizontal and vertical rupture extents are 4 and 11 km, respectively. (**B**) Stress drop and available strain energy as a function of rupture area radius. Assuming a rupture speed from 1.5 to 4.5 km/s, Ye *et al*. (*17*) obtained rupture radii of 1 to 3 km (thick black line), which correspond to stress drops higher than those of the 2013 Okhostk M_w 8.3 mainshock and the 1994 Bolivia earthquake (dashed blue lines as references, left vertical axis). The resulting available strain energy is also significantly higher than the radiated energy (dashed red line, right vertical axis) (*17*), which suggests low radiation efficiency. Our preferred result with a supershear rupture speed of 8 km/s is marked as the red dot, assuming a circular crack. The stress drop is about 32 MPa, and the available strain energy is close to the radiated energy, suggesting a radiation efficiency of near unity.

Previously identified extremely high-stress drops (157 MPa to 5.856 GPa) of the M_w 6.7 earthquake and subsequently low radiation efficiency ($0.005 < \eta_R < 0.15$) (*16*, *17*) depict this event as mechanistically distinct from the Okhotsk M_w 8.3 mainshock ($\Delta\sigma \approx 15$ MPa, $\eta_R \approx 0.6$) and more similar to the 1994 M_w 8.3 Bolivia earthquake ($\Delta\sigma \approx 114$ MPa, $\eta_R \leq 0.036$) in a warmer

slab (Fig. 4B). This complexity suggests strong stress heterogeneity in subducted slabs (*17*). However, supershear rupture during the M_w 6.7 earthquake brings its stress drop down to 32 MPa and its radiation efficiency to about 1.0 (Fig. 4B), which are much closer to values for the M_w 8.3 Okhotsk mainshock. Therefore, strong stress heterogeneity inside subducted slabs is not required to explain the 2013 Okhotsk mainshock and its M_w 6.7 aftershock. However, the difference in rupture speed (subshear versus supershear) indicates substantial spatial heterogeneity in the fracture strength or fracture energy within the slab.

Compared with shallow supershear events, this deep event has a relatively small rupture dimension and higher static stress drop (by a factor of ~10). Our estimate of high radiation efficiency ($\eta_R \approx 1.0$) during the M_w 6.7 event is also consistent with theoretical predictions of low fracture energy during supershear ruptures (*30*). This constraint of low fracture energy bears on the question of deep earthquake faulting mechanisms, which is still enigmatic (*15*, *19*). The 1994 Bolivia earthquake involved a large amount of fracture/thermal energy and radiated relatively little energy in seismic waves (*16*). In terms of energy partitioning, the supershear M_w 6.7 earthquake represents the opposite end member from the Bolivia earthquake, with almost all the available strain energy being radiated as seismic waves. This contrast is consistent with the idea of more than one rupture mechanism for deep earthquakes in slabs with different thermal states (*18*, *20*, *21*). The Okhotsk mainshock and aftershock in a cold slab ruptured with the transformational faulting mechanism, whereas the Bolivia earthquake in a warm slab was dominated by shear melting (*18*).

REFERENCES AND NOTES

1. R. Burridge, *Geophys. J. R. Astron. Soc.* **35**, 439–455 (1973).
2. D. Andrews, *J. Geophys. Res.* **81**, 5679–5687 (1976).
3. K. Xia, A. J. Rosakis, H. Kanamori, *Science* **303**, 1859–1861 (2004).
4. R. J. Archuleta, *J. Geophys. Res.* **89**, 4559–4585 (1984).
5. M. Bouchon *et al.*, *Geophys. Res. Lett.* **28**, 2723–2726 (2001).
6. M. Bouchon, M. Vallée, *Science* **301**, 824–826 (2003).
7. K. T. Walker, P. M. Shearer, *J. Geophys. Res.* **114** (B2), B02304 (2009).
8. M. Vallée, E. M. Dunham, *Geophys. Res. Lett.* **39**, L05311 (2012).
9. E. M. Dunham, R. J. Archuleta, *Bull. Seismol. Soc. Am.* **94**, S256–S268 (2004).
10. D. Wang, J. Mori, *Bull. Seismol. Soc. Am.* **102**, 301–308 (2012).
11. H. Yue *et al.*, *J. Geophys. Res.* **118**, 5903–5919 (2013).
12. M. Bouchon *et al.*, *Tectonophysics* **493**, 244–253 (2010).
13. H. Zhang, X. Chen, *Geophys. J. Int.* **167**, 917–932 (2006).
14. Y. Kaneko, N. Lapusta, *Tectonophysics* **493**, 272–284 (2010).
15. H. Houston, in *Treatise on Geophysics*, G. Schubert, Ed. (Elsevier, Amsterdam, 2007), pp. 321–350.
16. H. Kanamori, D. L. Anderson, T. H. Heaton, *Science* **279**, 839–842 (1998).
17. L. Ye, T. Lay, H. Kanamori, K. D. Koper, *Science* **341**, 1380–1384 (2013).
18. Z. Zhan, H. Kanamori, V. C. Tsai, D. V. Helmberger, S. Wei, *Earth Planet. Sci. Lett.* **385**, 89–96 (2014).
19. C. Frohlich, *Deep Earthquakes* (Cambridge Univ. Press, Cambridge, 2006).
20. D. A. Wiens, *Phys. Earth Planet. Inter.* **127**, 145–163 (2001).
21. R. Tibi, G. Bock, D. A. Wiens, *J. Geophys. Res.* **108**, 2091 (2003).
22. S.-C. Park, J. Mori, *J. Geophys. Res.* **113**, B08303 (2008).
23. M. Suzuki, Y. Yagi, *Geophys. Res. Lett.* **38**, L05308 (2011).
24. K. Kuge, *J. Geophys. Res.* **99** (B2), 2671–2685 (1994).
25. Z. Zhan, D. Helmberger, D. Li, *Phys. Earth Planet. Inter.* **232**, 30–35 (2014).
26. S. E. Persh, H. Houston, *J. Geophys. Res.* **109**, B04311 (2004).
27. A. Tocheport, L. Rivera, S. Chevrot, *J. Geophys. Res.* **112**, B07311 (2007).
28. Materials and methods are available in the supplementary materials.
29. C. J. Ammon *et al.*, *Science* **308**, 1133–1139 (2005).
30. R. Madariaga, K. B. Olsen, *Pure Appl. Geophys.* **157**, 1981–2001 (2000).
31. G. P. Hayes, D. J. Wald, R. L. Johnson, *J. Geophys. Res.* **117**, B01302 (2012).

ACKNOWLEDGMENTS

We thank two anonymous reviewers for their helpful comments. The Incorporated Research Institutions for Seismology (IRIS) provided the seismic data. This work was supported by NSF (grants EAR-1142020 and EAR-1111111). All data used are available from the IRIS data center at www.iris.edu.

SUPPLEMENTARY MATERIALS

www.sciencemag.org/content/345/6193/204/suppl/DC1
Materials and Methods
Figs. S1 to S9

27 February 2014; accepted 2 June 2014
10.1126/science.1252717

OCEAN MICROBES

Multispecies diel transcriptional oscillations in open ocean heterotrophic bacterial assemblages

Elizabeth A. Ottesen,[1,2,3] Curtis R. Young,[1,2] Scott M. Gifford,[1,2] John M. Eppley,[1,2] Roman Marin III,[4] Stephan C. Schuster,[5] Christopher A. Scholin,[4] Edward F. DeLong[1,2,6]*

Oscillating diurnal rhythms of gene transcription, metabolic activity, and behavior are found in all three domains of life. However, diel cycles in naturally occurring heterotrophic bacteria and archaea have rarely been observed. Here, we report time-resolved whole-genome transcriptome profiles of multiple, naturally occurring oceanic bacterial populations sampled in situ over 3 days. As anticipated, the cyanobacterial transcriptome exhibited pronounced diel periodicity. Unexpectedly, several different heterotrophic bacterioplankton groups also displayed diel cycling in many of their gene transcripts. Furthermore, diel oscillations in different heterotrophic bacterial groups suggested population-specific timing of peak transcript expression in a variety of metabolic gene suites. These staggered multispecies waves of diel gene transcription may influence both the tempo and the mode of matter and energy transformation in the sea.

The coordination of biological activities into daily periodic cycles is a common feature of eukaryotes and is widespread among plants, fungi, and animals, including man (*1*). Among single celled noneukaryotic microbes, diel cycles have been well documented in cyanobacterial isolates (*2*–*4*), one halophilic archaeon (*5*), and bacterial symbionts of fish and squid (*6*, *7*). Some evidence for diel cycling in microbial plankton has also been suggested on the basis of bulk community amino acid incorporation, viral production, or metabolite consumption (*8*–*10*). However, the existence of regular diel oscillations in free-living heterotrophic bacterial species has rarely been assessed.

Microbial community RNA sequencing techniques now allow simultaneous determination of whole-genome transcriptome profiles among multiple cooccurring species (*11*, *12*), enabling high-frequency, time-resolved analyses of microbial community dynamics (*12*, *13*). To better understand temporal transcriptional dynamics in oligotrophic bacterioplankton communities, we conducted a high-resolution multiday time series of bacterioplankton sampled from the North Pacific Subtropical Gyre (*14*).

To facilitate repeated sampling of the same planktonic microbial populations through time, automated Lagrangian sampling of bacterioplankton was performed every 2 hours over 3 days by using a free-drifting robotic Environmental Sample Processor (ESP) (*13*, *15*) (fig. S1). After instrument recovery, planktonic microbial RNA was extracted, purified, converted to cDNA, and sequenced to assess whole-genome transcriptome dynamics of predominant planktonic microbial populations (tables S1 and S2). The recovered cDNAs were dominated by transcripts from

[1]Department of Civil and Environmental Engineering, Massachusetts Institute of Technology, Cambridge, MA 02139, USA. [2]Center for Microbial Oceanography: Research and Education (C-MORE), University of Hawaii, Honolulu, HI 96822, USA. [3]Department of Microbiology, University of Georgia, Athens, GA 30602, USA. [4]Monterey Bay Aquarium Research Institute, Moss Landing, CA 95039, USA. [5]Singapore Centre on Environmental Life Sciences Engineering, Nanyang Technological University, 637551 Singapore. [6]Department of Biological Engineering, Massachusetts Institute of Technology, Cambridge, MA 02139, USA.
***Corresponding author. E-mail: edelong@hawaii.edu**